Local structure of $Ba(Ti,Zr)O_3$ perovskite-like solid solutions and its relation to the band-gap behavior

Igor Levin,[1] Eric Cockayne,[1] Victor Krayzman,[1] Joseph C. Woicik,[1] Soonil Lee,[2] and Clive A. Randall[2]
[1]*Ceramics Division, National Institute of Standards and Technology, Gaithersburg, Maryland 20899, USA*
[2]*Center for Dielectric Studies, Materials Research Institute, The Pennsylvania State University, University Park, Pennsylvania 16802, USA*
(Received 15 December 2010; published 30 March 2011)

Local structures in $BaTi_{1-x}Zr_xO_3$ solid solutions were analyzed using x-ray absorption fine structure (XAFS) measurements and density-functional theory (DFT) calculations. We demonstrate that for low concentrations of Ti, isolated Ti atoms in the relatively large octahedral sites of the $BaZrO_3$ lattice acquire centrosymmetric coordination with average Ti-O distances shorter than those in $BaTiO_3$. In contrast for higher concentrations of Ti, Ti atoms having one or more Ti as their B-site nearest neighbors undergo polar off-center displacements. Our DFT calculations confirm both effects. These results combined with the previously published data suggest that isolated polarizable ions on the B sites of a relatively expanded host perovskite lattice remain nonpolar by symmetric relaxation of the nearest-neighbor oxygen atoms to yield nearly ideal bond lengths around the dopant species. For neighboring Ti atoms, such symmetric relaxation is impossible, and these atoms are displaced off center. Our XAFS measurements did not detect any significant deviations from a random distribution of Ti and Zr in the present samples except for compositions close to $BaTiO_3$. The DFT calculations suggest that the dominant effect of the local displacements on band-gap values for this system is determined by the shortest Ti-O bonds due to strong Ti 3*d*–O 2*p* hybridization; however, local displacements have only a secondary effect on the band-gap behavior.

DOI: 10.1103/PhysRevB.83.094122 PACS number(s): 61.66.−f

I. INTRODUCTION

$Ba(Zr,Ti)O_3$ perovskite-like solid solutions exhibit dielectric and ferroelectric properties of interest for several technological applications[1–4] and have therefore attracted considerable attention. In this system the type of ferroelectric response (i.e., classical or relaxor) can be controlled by varying the Zr/Ti ratio. The end compound $BaTiO_3$ undergoes a complex sequence of phase transitions on cooling from the high-temperature paraelectric cubic polymorph to the tetragonal ($T_0 \approx 407$ K), orthorhombic ($T_0 \approx 285$ K), and rhombohedral ($T_0 \approx 189$ K) structures,[5] all of which are ferroelectric. Ti atoms exhibit random off-center ⟨111⟩-type displacements even in the cubic phase,[6,7] and these displacements order upon successive transitions to the lower-temperature ferroelectric polymorphs until complete ordering is attained in the rhombohedral structure.[6] (The disordered ⟨111⟩ displacements in the cubic phase are often referred to as the "eight-site model.") In contrast, the other end compound $BaZrO_3$ remains cubic down to at least 100 K (Ref. 8) with Zr cations located at centrosymmetric positions.

The local structures of concentrated $Ba(Ti,Zr)O_3$ solid solutions have been studied using various techniques, including Raman spectroscopy,[9–11] extended x-ray absorption fine structure measurements (EXAFS),[12] pair-distribution function from total neutron scattering,[13,14] and electron diffraction.[10] The results of studies using neutron total scattering and Zr *K*-edge EXAFS measurements agreed that the Zr-O and Ti-O bond distances in $Ba(Zr,Ti)O_3$ remain distinct and close to their values in the respective end compounds, as was also reported for the related $Ca(Ti,Zr)O_3$ system.[15] Analyses of the neutron PDF for the concentrated compositions[13,14] confirmed local polar Ti displacements similar to those encountered in $BaTiO_3$. The EXAFS study[12] suggested significant local segregation of Zr to form $BaZrO_3$-like clusters in a $BaTiO_3$-like matrix, and the random elastic fields associated with these clusters were speculated to be important for the relaxor properties. Recent studies of the optical band-gap, E_g, behavior in the $BaTi_{1-x}Zr_xO_3$ system[16] revealed a striking nonlinearity of the $E_g(x)$ dependence on both sides of the phase diagram; the compositional extent of the nonlinear region was significantly larger on the $BaZrO_3$ side. The observed nonlinearities in the band-gap behavior were tentatively attributed to local chemical segregation of Ti and Zr.[16] These results stimulated us to revisit the local structure of $BaTi_{1-x}Zr_xO_3$ solid solutions placing a particular emphasis on the structure of *dilute* compositions.

II. EXPERIMENTAL

Local structure measurements were performed on the same ceramic $BaTi_{1-x}Zr_xO_3$ samples ($x = 0$, 0.005, 0.02, 0.04, 0.12, 0.3, 0.5, 0.7, 0.9, 0.95, and 1) used for the optical band-gap study.[16] According to x-ray powder diffraction ($CuK\alpha_1$ radiation), the samples with $x = 0$ and $x = 0.005$ contain the tetragonal $BaTiO_3$ phase. The $x = 0.02$ sample contained a mixture of the tetragonal and orthorhombic structures, whereas the $x = 0.04$ sample contained primarily the orthorhombic phase. For $x \geqslant 0.12$, the structure was cubic. The dependence of lattice volume on composition was linear, as reported previously.[16]

XAFS measurements were conducted at ambient temperature at the NIST X23A2 beam line. For these measurements, finely ground powders (mortar and pestle) were dispersed on double-sided tape. The double-crystal monochromator was operated with a pair of Si(311) crystals. The data were collected in fluorescence and transmission for dilute and concentrated samples, respectively. A four-element Si-drift

detector was used for the fluorescence measurements. The detector count range was adjusted to minimize dead-time effects. Transmission data from the appropriate (Ti or Zr) metal foil positioned downstream from the sample were recorded simultaneously with each scan for calibration of energy. X-ray absorption near-edge structure (XANES) measurements for the Ti K edge were performed for compositions $x = 0$, 0.04, 0.12, 0.3, 0.5, 0.7, 0.90, and 0.95. (Measurements of Ti EXAFS were precluded by an overlap of the Ti K and Ba L_3 edges.) Good agreement between the transmission and fluorescence data was confirmed for the $x = 0.90$ sample. The Zr K-edge EXAFS data were collected for $x = 0.005$, 0.02, 0.04, 0.12, 0.5, 0.90, and 1. The $x = 0.12$ sample was used to verify agreement between the transmission and fluorescence data. All data were processed using ATHENA.[17] The fitting was accomplished using the ARTEMIS software package.[17] Scattering amplitudes and phases were calculated using FEFF8.20.[18]

III. COMPUTATIONAL STUDIES

The correlations between the local Ti/Zr distribution, local polar cation displacements, and the band gap were studied using density functional theory (DFT) calculations, as implemented in the code VASP.[19] Most calculations were performed on an 80-atom supercell with lattice vectors [022], [202], and [220]. The study used projector augmented wave pseudopotentials,[20,21] PBE parametrization[22] of the exchange correlation functional, and a k-point mesh equivalent to a 4×4×4 grid centered on the origin of the Brillouin zone for a primitive perovskite cell. Electronic wave functions were expanded in a plane-wave basis with a 354 eV cutoff for the wave functions and a 1500 eV augmentation charge cutoff. A composition-dependent artificial pressure was applied to correct for the DFT lattice parameter errors. The value of the artificial pressure was set such as to reproduce the experimental volumes at $x = 0$ and $x = 1$; a linear interpolation of these pressures was used for intermediate compositions. This correction is important because ionic displacements in ferroelectric systems are known to be very sensitive to the volume; furthermore, it has been noted empirically that better predictions of ionic displacements can often be obtained using the experimental volume rather than the fully self-consistent DFT volume.[23] Various compositions and Zr/Ti distributions were tested. Ti atoms were initially displaced along $\langle 111\rangle_c$-type directions based on the experimental evidence cited above for local Ti displacements in Ba(Ti,Zr)O_3,[6,7] but all atoms were subsequently allowed to relax.

IV. RESULTS AND DISCUSSION

A. Local Ti coordination from Ti K preedge structure and DFT calculations

The Ti K pre-edge structure [Fig. 1(a), features A, B, and C] contains rich information on the local Ti coordination environment.[24] The integrated intensity under peak B, which is associated with both the quadrupole and the dipole $1s \rightarrow 3d$ transitions, reflects the $3d$-$4p$ hybridization for Ti and is directly proportional to the mean-squared displacements of Ti

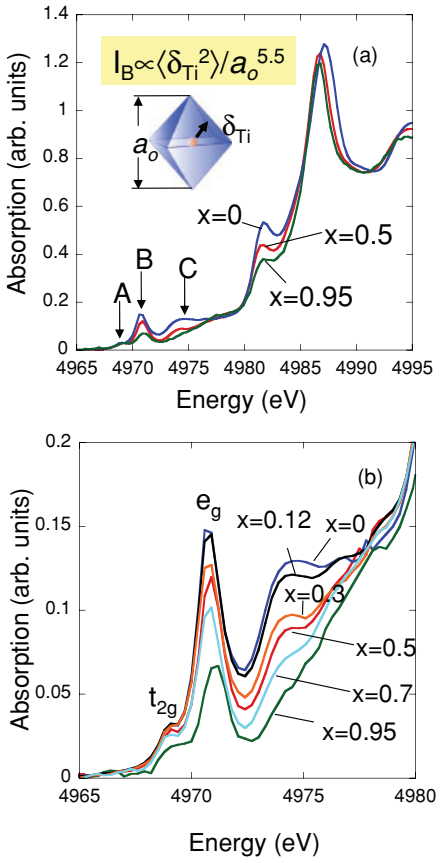

FIG. 1. (Color online) X-ray absorption Ti K preedge structure for Ba(Ti,Zr)O_3 samples. (a) The preedge features for selected compositions are indicated as A, B, and C. The intensity of feature B is related to the off-center Ti displacements whereas the intensity of feature C is determined by the local Zr/Ti ratio around the absorbing Ti (Ref. 21). (b) Ti preedge structure for all measured compositions. Note systematic variation in the intensities of features B and C.

off the instantaneous centers of oxygen octahedra according to[24]

$$I_B \propto \frac{\langle \delta_{\mathrm{Ti}}^2 \rangle}{a_0^{5.5}}, \tag{1}$$

where δ_{Ti} is the magnitude of the local off-center Ti displacements and a_0 is the size of the corresponding oxygen octahedron (Fig. 1). The intensity of this peak decreases progressively upon Zr substitution into $BaTiO_3$ [Figs. 1(b) and 2(a) with a pronounced drop observed for the Zr fraction increasing from $x = 0.7$ to $x = 0.9$ (Fig. 2). This trend cannot be accounted for by the expansion of a_0 [Fig. 2(a)], even if the a_0 values are equated with the average lattice parameters, which is obviously a gross overestimation of the volume of the [TiO_6] octahedra. Thus, despite a linear expansion of the lattice volume with increasing x, the magnitude of local Ti off-center displacements in the $BaTi_{1-x}Zr_xO_3$ solid solutions decreases dramatically when x values exceed 0.4. A noticeable upshift of peak B is observed for $x > 0.7$ [Fig. 1(b)] which indicates the shortening of Ti-O bond distances for the low concentrations of Ti in $BaZrO_3$, consistent with the reduced off-center Ti displacements. Comparison of the Ti K pre-edge structure for $BaTi_{0.05}Zr_{0.95}O_3$ and $CaTiO_3$ (unit cell volume $V \approx 56.02$ Å^3

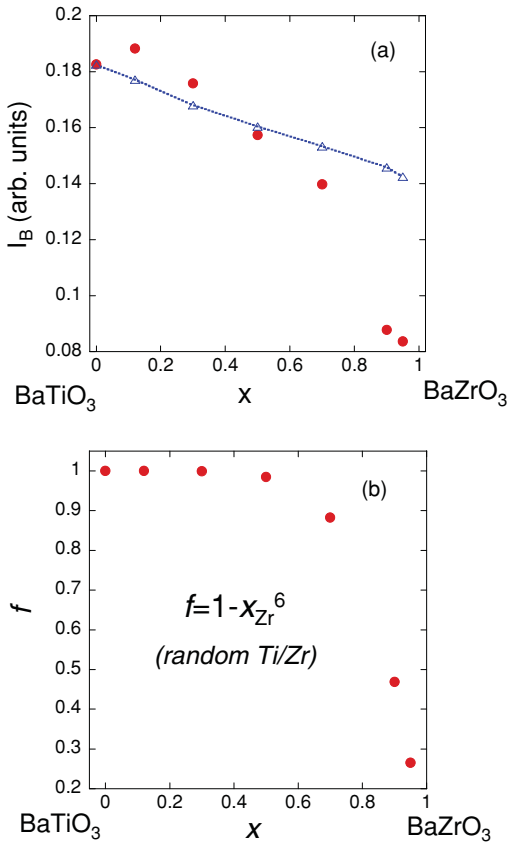

FIG. 2. (Color online) (a) Compositional dependence of the integrated intensity under the Ti *K* preedge peak B (red/circles). The blue dashed line/triangles indicate reduction in the intensity of peak B according to the $a_0^{5.5}$ term in Eq. (1) if a_0 is equated with the x-ray lattice parameter. (b) Calculated compositional dependence of the fraction *f* of Ti having one or more Ti as a next-nearest neighbor for a random distribution of Ti and Zr on the B sites.

for a five-atom perovskite cell), where Ti reportedly resides in the inversion centers, suggests a similar nonpolar behavior for dilute concentrations of Ti in the relatively large octahedral sites of $BaZrO_3$ (unit cell volume $V \approx 73.85$ Å^3) (Fig. 3). The area under feature C is proportional to the local Ti/Zr

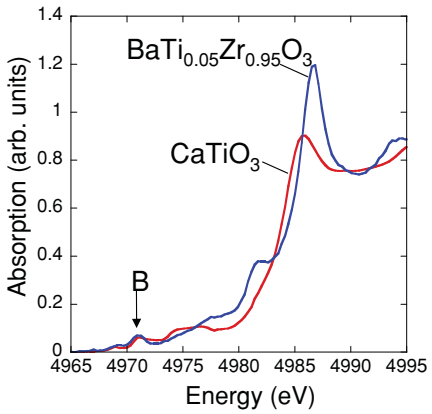

FIG. 3. (Color online) Comparison of the Ti *K* preedge structure in $BaTi_{0.05}Zr_{0.95}O_3$ and $CaTiO_3$. Note similar intensities of feature B in the two samples.

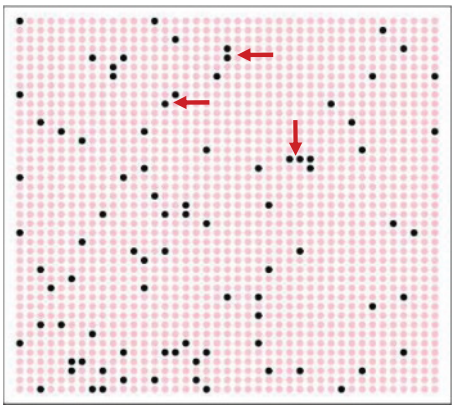

FIG. 4. (Color online) (a) Schematic drawing illustrating a random distribution of 5% of dopant species (black) on the sites of the square host lattice (red). Most dopant atoms are isolated with a small fraction of dopant-dopant nearest-neighbor pairs indicated using arrows.

ratio around Ti.[24,25] Systematic changes in the intensity of this feature among the $BaTi_{1-x}Zr_xO_3$ samples [Fig. 1(b)] rule out any significant short-range ordering/clustering of Ti and Zr, defined according to Warren.[26]

The absence of off-center Ti displacements in $BaTi_{0.05}Zr_{0.95}O_3$, as inferred from the Ti preedge x-ray absorption structure, suggests that the isolated Ti atoms in $BaZrO_3$ attract their oxygen neighbors to adopt nearly ideal Ti-O bond lengths (i.e., bond valence 2/3 v.u. (valence units)) at the expense of stretched Zr-O bonds in nearest-neighboring [ZrO_6] octahedra. This effect can be attributed to stronger Ti-O bonds as compared to Zr-O bonds. Random distribution of Ti in $BaZrO_3$ inevitably yields a certain fraction of Ti-Ti neighbors (Fig. 4) even for dilute solid solutions. In this case, oxygen atoms in the Ti-O-Ti links cannot satisfy the bonding requirements of both competing Ti atoms, which leads to stretched Ti-O bonds and off-center displacements of Ti. Such polar clusters are consistent with previous dielectric and Raman measurements[11] on Ti-substituted $BaZrO_3$; apparently, small fractions of polar clusters for dilute concentrations of Ti remain undetected in the preedge x-ray absorption structure. For a random Zr/Ti distribution, the fraction *f* of [TiO_6] octahedra having one or more [TiO_6] octahedra as a nearest neighbor can be calculated as $1-x^6$, where *x* is the fraction of Zr [Fig. 2(b)]. The dependence $f(x)$ resembles the trend observed for the integrated intensity of peak B and is consistent with the intensity of this peak increasing with the fraction of polar Ti atoms in the sample.

DFT calculations (Fig. 5) reproduce the tendency for isolated Ti atoms in $BaZrO_3$ to adopt centrosymmetric environments, while Ti atoms having at least one Ti as their nearest B-site neighbor move off center. This was confirmed in calculations comparing two 80-atom supercells, one containing a single Ti ion [Fig. 5(a)] and another with a pair of neighboring Ti [Fig. 5(b)]. Oxygen atoms around an isolated Ti atom relax symmetrically toward this Ti and away from the neighboring Zr atoms. For configurations containing Ti pair clusters, a symmetric oxygen relaxation around both Ti sites is impossible, and Ti atoms move off center. The polar-cluster configuration presented in Fig. 5(b), which

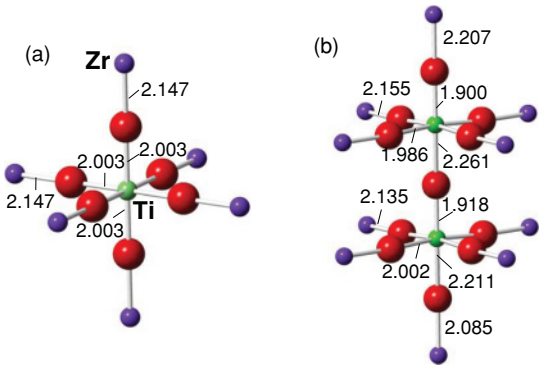

FIG. 5. (Color online) Local oxygen (red spheres) coordination of Ti ions (green spheres) found in $Ba(Ti,Zr)O_3$ via density functional theory (DFT) calculations. Zr cations are indicated using purple spheres. Ti-O and Zr-O bond lengths are given in Å. (a) An isolated Ti ion in $BaZrO_3$ and (b) a pair of neighboring Ti ions that form a polar cluster. Due to local tetragonal symmetry, all equatorial bond lengths in (b) are equal. The ferroelectric arrangement is found to be more stable than the paraelectric one.

features parallel Ti displacements, is more stable than that with antiparallel displacements (not shown). The magnitude of Ti displacements is larger for the polar cluster. The calculated mean Ti-O distance expands from 2.004 Å to 2.011 Å upon Ti off centering by ≈0.084 Å [Fig. 5(b)], but the displacements decrease the length of the shortest Ti-O bonds. For configurations shown in Fig. 5, the Ti atoms were initially displaced along ⟨111⟩, but relaxation yields structures with local cubic [Fig. 5(a)] and tetragonal [Fig. 5(b)] symmetries. Isolated Ti atoms [Fig. 5(a)] relax to the centrosymmetric position whereas near-neighbor pairs of Ti [Fig. 5(b)] exhibit parallel ⟨001⟩ displacements. These directions of Ti displacements contrast with ⟨111⟩ Ti displacements in pure $BaTiO_3$; both experimental measurements and theoretical calculations agree that the most stable directions for Ti displacement in $BaTiO_3$ are ⟨111⟩. Thus, our results indicate that the eight-site model[6] needs to be modified for dilute Ti concentrations in $BaZrO_3$. These findings are consistent with the results of recent first-principles calculations for $BaTi_{0.74}Zr_{0.26}O_3$ (Ref. 27) which suggests that the directions and magnitudes of Ti off-center displacements are determined by the local Ti/Zr concentration around the Ti atoms.

B. Zr K-edge EXAFS: Local distribution of Ti and Zr

The Zr *K*-edge EXAFS data for selected $BaTi_{1-x}Zr_xO_3$ compositions are summarized in Fig. 6. For all compositions, a simple perovskite model featuring linear Zr-O-Zr and Zr-O-Ti links, as in the cubic $BaZrO_3$ structure, was tested. The photoelectron single- and multiple-scattering paths used in the fit are summarized in Table I. The interatomic distances and their associated Debye-Waller factors were constrained to minimize the number of independent structural variables (Table I). The probability (α) of finding a Zr atom in the third coordination shell around the absorbing Zr was refined to evaluate local atomic ordering/clustering. The examples of fits for selected samples are displayed in Fig. 6 and the refined structural parameters are summarized in Table II. Clearly, a simple model with chemically sound values of the structural

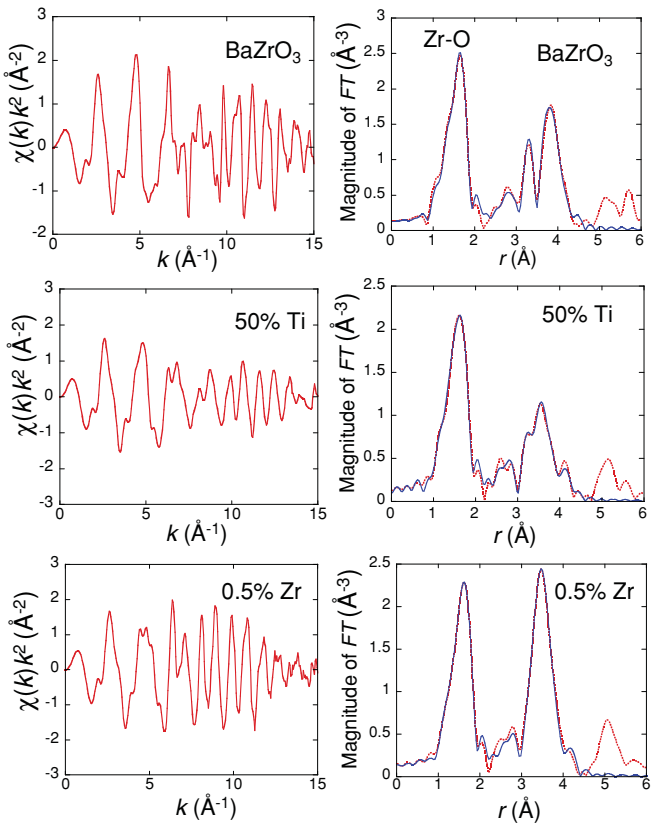

FIG. 6. (Color online) Examples of Zr EXAFS fits for selected compositions using the model described in Table I. The EXAFS data (left) were weighted by k^2 prior to a Fourier transform (FT). The k range used in FT was from ≈2.25 $Å^{-1}$ to ≈ 14 $Å^{-1}$.

variables is sufficient to describe the experimental data in the entire composition range.

The Zr-O distances change relatively little with the Zr/Ti ratio [Fig. 7(a)]; however, for dilute concentrations of Zr in $BaTiO_3$, these distances are slightly shorter compared to their values in the concentrated solid solutions. For example, the Zr-O distance changes from 2.103(4) Å in $BaZrO_3$ to 2.088(3) Å in the samples with low concentrations of Zr in $BaTiO_3$. The Zr-Ba distances [Fig. 7(a)] decrease markedly with decreasing Zr content. The analyses yield statistical values of the occupational probability α for all compositions except those close to $BaTiO_3$ ($x = 0.005$, 0.02, and 0.04), where a small, yet significant (with respect to the estimated standard uncertainty) Zr clustering is observed. The actual significance of this weak clustering can be questioned considering the approximations of the model and the fact that the parameter uncertainties, as estimated by ARTEMIS, provide lower bounds for the errors. Clustering of Zr for compositions in the vicinity of $BaTiO_3$ is also suggested by the mixtures of tetragonal and orthorhombic $BaTiO_3$-based polymorphs revealed in these samples by x-ray diffraction; however, the scale of these heterogeneities, as reflected in the size of coherently scattering domains seen by x-ray diffraction (inferred from the width of reflections), is at least an order of magnitude larger than the distance range probed by EXAFS.

Our results contrast with the previously published EXAFS studies of the concentrated $Ba(Zr,Ti)O_3$ solid solutions which

TABLE I. Photoelectron scattering paths used to fit the Zr *K*-edge EXAFS data for the $BaZr_{1-x}Ti_xO_3$ solid solutions. N, R_{eff}, and σ specify the number of equivalent paths, effective path length, and Debye-Waller factor, respectively, for each path. Symbol "↔" denotes single-scattering paths. Parameter α represents a probability of finding a Zr atom in the third coordination shell around the absorber.

Path	Scattering	N	R_{eff}	σ
1	$Zr_c \leftrightarrow O_1$	6	R_{ZrO}	σ_{ZrO}
2	$Zr_c \leftrightarrow Ba$	8	R_{ZrBa}	σ_{ZrBa}
3′	$Zr_c \leftrightarrow Zr$	$6 \times \alpha$	$2 \times R_{ZrO}$	σ_{ZrZr}
3′	$Zr_c \leftrightarrow Ti$	$6 \times (1-\alpha)$	$(R_{ZrO} + R_{TiO})$	σ_{ZrZr}
4	$Zr_c \rightarrow Zr \rightarrow O_1 \rightarrow Zr_c$	$12 \times \alpha$	$2 \times R_{ZrO}$	σ_{ms}
4′	$Zr_c \rightarrow Ti \rightarrow O_1 \rightarrow Zr_c$	$12 \times (1-\alpha)$	$(R_{ZrO} + R_{TiO})$	σ_{ms}
5	$Zr_c \rightarrow O_1 \rightarrow Zr \rightarrow O_1 \rightarrow Zr_c$	$6 \times \alpha$	$2 \times R_{ZrO}$	σ_{ms}
5′	$Zr_c \rightarrow O_1 \rightarrow Ti \rightarrow O_1 \rightarrow Zr_c$	$6 \times (1-\alpha)$	$(R_{ZrO} + R_{TiO})$	σ_{ms}
6	$Zr_c \rightarrow O_1 \rightarrow Zr_c \rightarrow O_1 \rightarrow Zr_c$	6	$2 \times R_{ZrO}$	$2 \times \sigma_{ZrO}$
7	$Zr_c \rightarrow O_1 \rightarrow Zr_c \rightarrow O_1 \rightarrow Zr_c$	6	$2 \times R_{ZrO}$	$2 \times \sigma_{ZrO}$
8	$Zr_c \rightarrow O_1 \rightarrow O_1' \rightarrow Zr_c$	6	$2 \times R_{ZrO}$	$2 \times \sigma_{ZrO}$
9	$Zr_c \leftrightarrow O_2$	24	$R_{ZrO(2)}$	$\sigma_{ZrO(2)}$

suggested significant segregation of Zr accompanied by strong buckling of the B-O-B bonds in the Zr-rich clusters. In those studies, fitting an idealized model with linear B-O-B links [but a larger number of independent Debye-Waller (D-W) factors than used in the present study] produced unphysical values of σ_{ms} (defined in Table I) and, therefore, a more complex model with buckled Zr-O-Zr and Zr-O-Ti links was introduced (the two buckling angles have been refined as independent variables). In the present case, a simple model provides a satisfactory fit to the data with sound values for all the refined variables and, therefore, introducing a more complex model having a larger number of free parameters is not justified. Comparison of the presently refined Zr-O and Zr-Ba bond distances indeed suggests significant buckling of the Zr-O-Zr links in the $x = 0.5$ sample. According to previous studies of local structures in Ca(Zr,Ti)O_3,[15] this buckling is the primary mechanism for accommodating B-cation size mismatch in disordered perovskite solid solutions. Our XAFS data indicate no significant local segregation of Zr/Ti in the $x = 0.5$ sample under the presently used processing conditions.

C. Local distances from EXAFS and x-ray diffraction

Comparison of local cation-oxygen and cation-cation distances in a perovskite structure is facilitated by considering effective cubic lattice parameters that correspond to each of these distances because such lattice parameters can be plotted on the same scale. Figure 7(b) summarizes effective values of the cubic lattice parameters $a_{Zr\text{-}O}$ and $a_{Zr\text{-}Ba}$ calculated from the Zr-O and Zr-Ba distances ($a_{Zr\text{-}O} = 2 \times |Zr\text{-}O|$) and $a_{Zr\text{-}Ba} = |Zr\text{-}Ba| \times 2/\sqrt{3}$), respectively, determined from EXAFS, and the average lattice parameters a_{XRD} obtained from x-ray diffraction. Additionally, the effective cubic lattice parameters corresponding to the Ti-O and Ti-Ba distances were estimated according to $a_{XRD} = x a_{Zr\text{-}O} + (1-x) a_{Ti\text{-}O}$ and $a_{XRD} = x a_{Zr\text{-}Ba} + (1-x) a_{Ti\text{-}Ba}$, respectively [Fig. 7(b)]. From these estimates, the Ti-O bond distance expands slightly with Zr content increasing from $x = 0$ to $x = 0.5$ and then decreases for dilute concentrations of Ti in $BaZrO_3$ to a value smaller than that observed in $BaTiO_3$ [Fig. 7(b)]; note, however, that the uncertainties for the estimated Ti-O and Ti-Ba distances increase as $1/(1-x)$. Thus, the results obtained from the Zr *K*-edge EXAFS are entirely consistent with the inferences from the Ti *K* preedge data. Likewise, the estimated trends for the Ti-O distances agree with the theoretical predictions discussed above.

The average Ti-O distance in the $x = 0.5$ sample is estimated to be at least as long as encountered in $BaTiO_3$ [Fig. 7(b)], whereas the local off-center Ti displacements in the solid solution samples are considerably smaller compared to the end compound. Presumably, the magnitude of Ti displacements is affected not only by the Ti-O bond length but also by the strength of correlations among the Ti-Ti displacements, as manifested in diffuse intensity sheets in electron/x-ray

TABLE II. Parameters of the Zr coordination environment in $BaZr_{1-x}Ti_xO_3$ obtained by fitting the Zr EXAFS data up to 4.3 Å.

x	α	R_{ZrO} (Å)	R_{ZrBa} (Å)	R_{TiO} (Å)	$R_{ZrO(2)}$ (Å)	s_{ZrO} (Å^2)	σ_{ZrBa} (Å^2)	σ_{ZrZr} (Å^2)	σ_{ms} (Å^2)	$\sigma_{ZrO(2)}$ (Å^2)	R (%)
1.00	1.00	2.103(4)	3.646(5)	N/A	4.71(2)	0.003(1)	0.0065(4)	0.005(2)	0.005(2)	0.009(3)	1.3
0.90	0.91(7)	2.101(3)	3.637(6)	2.10(8)	4.70(2)	0.003(1)	0.007(1)	0.003(1)	0.004(1)	0.010(4)	1.5
0.50	0.58(7)	2.093(3)	3.588(4)	2.02(1)	4.63(2)	0.005(1)	0.007(1)	0.003(1)	0.006(1)	0.013(3)	1.5
0.12	0.19(8)	2.092(4)	3.542(4)	1.98(1)	4.56(2)	0.005(1)	0.0058(4)	0.003(1)	0.006(2)	0.010(2)	1.6
0.04	0.11(6)	2.088(3)	3.528(3)	1.973(8)	4.53(1)	0.004(1)	0.0048(4)	0.003(1)	0.005(2)	0.008(2)	0.64
0.02	0.12(6)	2.086(4)	3.529(3)	1.968(7)	4.53(1)	0.004(1)	0.0050(3)	0.003(1)	0.005(2)	0.008(2)	0.81
0.005	0.14(5)	2.088(3)	3.530(2)	1.977(6)	4.53(1)	0.004(1)	0.0052(3)	0.005(1)	0.005(3)	0.010(2)	0.67

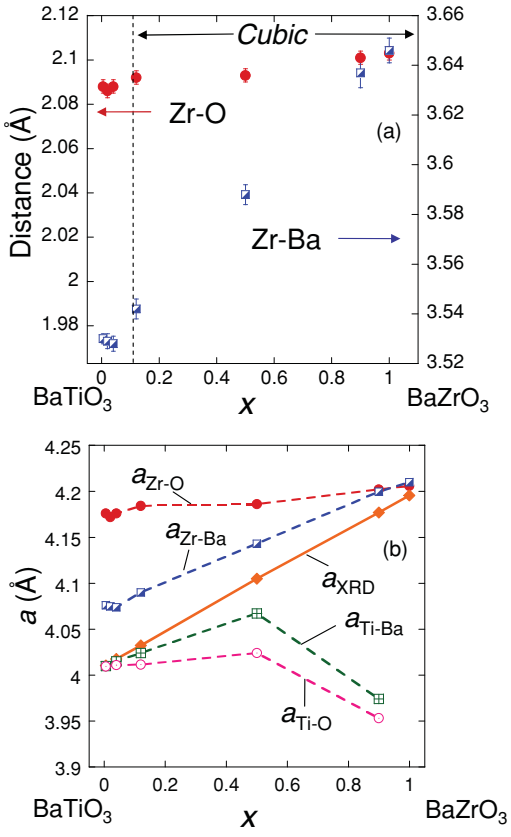

FIG. 7. (Color online) (a) Compositional dependence of the Zr-O and Zr-Ba distances obtained by fitting the EXAFS data. (b) Compositional dependence of the effective lattice parameters $a_{\text{Zr-O}}$ and $a_{\text{Zr-Ba}}$ calculated using the local Zr-O ($a_{\text{Zr-O}} = 2 \times |\text{Zr-O}|$) and Zr-Ba($a_{\text{Zr-Ba}} = |\text{Zr-Ba}| \times 2/\sqrt{3}$) distances, respectively, as obtained by fitting the Zr EXAFS data. The compositional dependence of the x-ray lattice parameter is superimposed. The analogous effective lattice parameters corresponding to the Ti-O and Ti-Ba distances were estimated as $a_{\text{Ti-O}} = (a_{\text{XRD}} - a_{\text{Zr-O}} \times x)/(1-x)$ and $a_{\text{Ti-Ba}} = (a_{\text{XRD}} - a_{\text{Zr-Ba}} \times x)/(1-x)$, respectively.

diffraction,[7,10] which are expected to be weaker in the $x = 0.5$ sample as compared to $BaTiO_3$.

D. Local structure and band-gap behavior

Our theoretical calculations confirm that the top of the valence band and the bottom of the conduction band are determined by the nonbonding O $2p$ (at the R point) and antibonding Ti $3d$–O $2p$ (or Zr $4d$–O $2p$ for $BaZrO_3$) t_{2g}-like orbitals (at the Γ point), respectively.[28] The addition of Ti to $BaZrO_3$ introduces Ti t_{2g} states that lie below Zr $4d$ and thus reduce the band gap compared to pure $BaZrO_3$. Preliminary DFT results reproduce the nonlinear decrease of the band gap with increasing Ti concentration in the $BaZrO_3$-rich part of the diagram (Fig. 8) and indicate that this trend is independent of local structure. For concentrated solid solutions (not shown in Fig. 8), we find a significant dependence of the calculated band gap on the local environment of the B ions; however, it remains unclear how to calculate an ensemble average for the band gap.

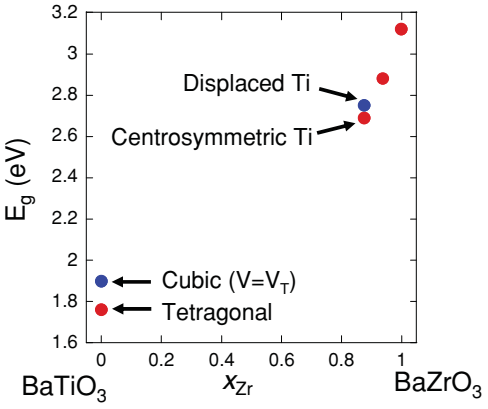

FIG. 8. (Color online) Calculated band-gap values in $BaTi_{1-x}Zr_xO_3$ for $x = 0$, 0.875, 0.9375, and 1. For $x = 0$, two configurations were considered: a tetragonal (red) having lattice parameters fixed at the experimental values and a cubic (blue) having the same volume as the tetragonal structure. These configurations are shown in Fig. 9. For $x = 0.875$, the band gap was also calculated for the two distinct configurations: configuration I (red) with isolated centrosymmetric Ti atoms and configuration II (blue) with displaced Ti being nearest B-site neighbors (Fig. 5). For $x = 0.9375$, the only possible configuration included an isolated centrosymmetric Ti atom (Fig. 5).

Nonetheless, calculations do show that local structure has some effect on the band gap at a fixed composition. We demonstrate this by comparing two 80-atom supercells with lattice vectors as described above, and identical compositions $(1-x) = 0.125$. In configuration I, the two Ti atoms are placed at positions (000) and $(\frac{1}{2}\ \frac{1}{2}\ \frac{1}{2})$ in the coordinates of the supercell. The minimum Ti-Ti separation is about $2a$, and the relaxed local geometry is similar to that in Fig. 5(a). In configuration II, the 2 Ti atoms are placed at positions (000) and $(\frac{1}{4}\frac{1}{4}\frac{1}{4})$. The minimum Ti-Ti separation is about a, and the relaxed geometry is shown in Fig. 5(b). The calculated band gap increases from 2.69 to 2.75 eV on going from the "isolated Ti" case to the "neighboring Ti" case (Fig. 8). (Calculated DFT band gaps are well known to be smaller than the experimental values, but the trends that we find are expected to be valid.) The average Ti-O distance expands from 2.007 Å for isolated Ti to 2.011 Å for

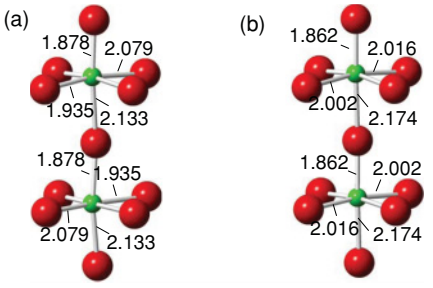

FIG. 9. (Color online) DFT local structures for $BaTiO_3$ that demonstrate the effect of increasing tetragonality on the local structure: (a) lattice parameter ratio $c/a = 1$ and (b) lattice parameters a and c are fixed at the experimental values. In each case, the initial Ti displacements are along nonequivalent ⟨111⟩ directions, as described in the text.

Ti with neighboring Ti configurations, similar to the increase of the average bond distance with increasing Ti concentration. Inspection of the electronic structure shows that the larger band gap for configuration II is due to the formation of short Ti-O bonds caused by ferroelectric-type displacements of Ti. Shorter Ti-O distances increase Ti $3d$ –O $2p$ hybridization and increase the band gap compared to its value without ferroelectric-type local distortion. Although the fraction of off-centered Ti atoms increases with increasing Ti concentration, as described above, the effect of increasing local Ti-O hybridization is not enough to overcome the dominant trend of decreasing band gap with increasing Ti concentration. For comparison, the calculated band gap decreases from 3.12 eV for $BaZrO_3$ to 2.88 eV for a configuration with one isolated Ti atom (centrosymmetric coordination) per 80-atom supercell to 2.69 eV for a configuration with two isolated Ti atoms (centrosymmetric coordination) per 80-atom supercell (Fig. 8).

The origin of the abrupt decrease in the band gap with increasing Ti concentration in the vicinity of $BaTiO_3$ is not intuitive. According to our theoretical calculations, these changes can be attributed at least in part to the increasing tetragonality (c/a ratio) as $BaTiO_3$ is approached (Figs. 8 and 9). The calculations were performed for two $BaTiO_3$ configurations: The first model adopted the experimental values of lattice parameters a and c, whereas the second model assumed $a = c = V^{1/3}$, where V is the experimental volume of $BaTiO_3$. In each case, Ti atoms were displaced randomly along 4 nonequivalent ⟨111⟩ directions. This configuration simulates the Ti-Ti correlations in the tetragonal phase, consistent with the partially ordered four-site model. As seen in Fig. 9, both correlations of Ti displacements along the c direction and the distorted c/a ratio tend to reorient the Ti displacements from ⟨111⟩-type directions to ⟨xxz⟩ directions. The calculated band gap decreased from 1.90 eV for the cubic cell to 1.76 eV for the tetragonal cell. This change in the band gap arises because the tetragonality of the cell aligns the Ti displacements more along the c axis and further away from the ⟨111⟩ directions. Ti displacements along ⟨111⟩ directions yield three short Ti-O distances, as opposed to one short distance for nearly [001]-type displacements (Fig. 9); therefore, the cubic cell with displacements closer to the ⟨111⟩ directions exhibits stronger Ti $3d$–O $2p$ hybridization and a larger band gap. The decreased tetragonality with the tetragonal to cubic transition raises the conduction band as much as it lowers the valence band. An alternate hypothesis for the rapid change in band gap with Zr concentration in Ti-rich Ba(Ti,Zr)O_3 is that Zr $4d$ states play a role in the band gap; however, calculations revealed no special involvement of Zr in the highest valence bands and lowest conduction bands.

Despite the above discussion, experimental results demonstrate that substitution of 0.5% Zr in $BaTiO_3$ only weakly affects the c/a ratio [1.0109(3) in $BaTiO_3$ versus 1.0106(3) in the doped sample] whereas the band gap changes by nearly 0.1 eV.[16] Analysis of real samples is complicated by a heterogeneous distribution of Zr and Ti, yielding a mixture of tetragonal and orthorhombic structures for dilute concentrations of Zr in $BaTiO_3$; this renders direct comparison with theoretical calculations that rely on relatively idealized models somewhat difficult. Since Ba(Ti,Zr)O_3 solid solutions are indirect band-gap materials, the band-gap values deduced from optical absorption can also be affected by phonon contributions. Further experimental and theoretical studies are warranted to ascertain the exact reasons for the band-gap nonlinearity in the $BaTiO_3$-rich part of the system.

V. SUMMARY

Our results demonstrate that isolated Ti atoms placed in the relatively large octahedral sites in $BaZrO_3$ ($V \approx 73.85$ Å^3) acquire centrosymmetric environments as opposed to the off-centered Ti atoms in the smaller $BaTiO_3$ ($V \approx 64.49$ Å^3) lattice. The average Ti-O distances for the isolated Ti atoms in $BaZrO_3$ are shorter than those in $BaTiO_3$. Increasing Ti concentrations in $BaZrO_3$ introduce Ti-Ti B-site neighbors which exhibit polar off-center displacements, thereby increasing the mean Ti-O distance until this dependence flattens for Ti concentrations greater than 30%. Zr-O distances in Ba(Ti,Zr)O_3 solid solutions remain similar to their values in $BaZrO_3$ but shorten slightly for dilute concentrations of Zr in $BaTiO_3$. XAFS analyses reveal no detectable Zr/Ti segregation in the present samples except for compositions close to $BaTiO_3$. First-principles calculations corroborate the structural trends inferred from the XAFS data and establish some correlations between the local structure and band-gap behavior. However, comprehensive understanding of the band-gap behavior in this system requires additional work.

Recent studies of Mn-doped (<2% Mn) $SrTiO_3$ revealed that Mn^{4+} cations ($R = 0.53$ Å) on the Ti ($R = 0.605$ Å) sites adopt nearly ideal Mn-O distances which are appreciably shorter than the Ti-O distances.[29] Therefore, despite their smaller size relative to the host lattice, Mn^{4+} cations remain central and the samples exhibit no dielectric anomalies. In fact, Mn behavior on the B sites in $SrTiO_3$ is analogous to that of Ti in $BaZrO_3$. In contrast, when Mn at similar concentrations is incorporated into large Sr sites (as Mn^{2+}), Mn cations are strongly displaced off center leading to dielectric relaxation. We conjecture that isolated transition-metal cations in the octahedral B sites of a relatively large host perovskite lattice remain nonpolar by pulling the oxygen atoms away from the neighboring host B cations to attain six nearly ideal metal-oxygen bond lengths. Thus, relatively large concentrations of dopant atoms are needed to generate numbers of dopant-dopant pairs sufficient for a noticeable polar behavior. In contrast, A-site substitutions cannot accommodate their bonding requirements via symmetric relaxation of the oxygen atoms and thus strong off centering of these cations and the associated polar-type response are obtained even for very dilute concentrations of the dopant species.

[1]D. F. K. Hennings, B. Schreinemacher, and H. Shcreinemacher, J. Eur. Ceram. Soc. **13**, 81 (1994).

[2]Z. Yu, C. Ang, R. Guo, and A. S. Bhalla, J. Appl. Phys. **92**, 1489 (2002).

[3]T. Maiti, R. Guo, and A. S. Bhalla, J. Am. Ceram. Soc. **91**, 1769 (2008).
[4]A. Simon, J. Ravez, and M. Maglione, J. Phys.: Condens. Matter **16**, 963 (2004).
[5]H. D. Megaw, *Crystal Structures: A Working Approach* (Saunders, Philadelphia, 1973).
[6]R. Comes, M. Lambert, and A. Guinier, Solid State Commun. **6**, 715 (1968).
[7]B. Ravel, E. A. Stern, R. I. Vedrinskii, and V. Kraizman, Ferroelectrics **206**, 407 (1998).
[8]I. Levin, T. G. Amos, S. M. Bell, L. Farber, T. A. Vanderah, R. S. Roth, and B. H. Toby, J. Solid State Chem. **175**, 170 (2003).
[9]R. Farhi, M. El Marssi, A. Simon, and J. Ravez, Eur. Phys. J. B **9**, 599 (1999).
[10]S. Miao, J. Pokorny, U. M. Pasha, O. P. Thakur, D. C. Sinclair, and I. M. Reaney, J. Appl. Phys. **106,** 114111 (2009).
[11]N. K. Karan, R. S. Katiyar, T. Maiti, R. Guo, and A. S. Bhalla, J. Raman Spectrosc. **40**, 370 (2009).
[12]C. Laulhe, F. Hippert, J. Kreisel, M. Maglione, A. Simon, J. L. Hazemann, and V. Nassif, Phys. Rev. B **74**, 014106 (2006).
[13]C. Laulhe, F. Hippert, R. Bellissent, A. Simon, and G. J. Cuello, Phys. Rev. B **79**, 064104 (2009).
[14]I. K. Jeong, C. Y. Park, J. S. Ahn, S. Park, and D. J. Kim, Phys. Rev. B **81**, 214119 (2010).
[15]I. Levin, E. Cockayne, M. W. Lufaso, J. C. Woicik, and J. E. Maslar, Chem. Mater. **18**, 854 (2006).
[16]S. Lee, R. Levi, W. Qu, S. C. Lee, and C. A. Randall, J. Appl. Phys. **107**, 023523 (2010).
[17]B. Ravel and M. Newville, J. Synchrotron Radiat. **12**, 537 (2005).
[18]S. I. Zabinsky, J. J. Rehr, A. Ankudinov, R. C. Albers, and M. J. Eller, Phys. Rev. B **52**, 2995 (1995).
[19]G. Kresse and J. Furthmuller, Phys. Rev. B **54**, 11169 (1996).
[20]P. E. Blochl, Phys. Rev. B **50**, 17953 (1994).
[21]G. Kresse and D. Joubert, Phys. Rev. B **59**, 1758 (1999).
[22]J. P. Perdew, K. Burke, and M. Ernzehof, Phys. Rev. Lett. **77**, 3865 (1996).
[23]R. E. Cohen, Nature (London) **358**(6382), 136 (1992).
[24]R. V. Vedrinskii, V. L. Kraizman, A. A. Novakovich, P. V. Demekhin, and S. V. Urazhdin, J. Phys.: Condens. Matter **10**, 9561 (1998).
[25]V. Krayzman, I. Levin, J. C. Woicik, D. Yoder, and D. A. Fischer, Phys. Rev. B **74**, 224104 (2006).
[26]B. E. Warren, *X-ray Diffraction* (Dover, New York, 1969).
[27]C. Laulhe, A. Pasturel, F. Hippert, and J. Kreisel, Phys. Rev. B **82**, 132102 (2010).
[28]F. M. Michel-Calendini and G. Mesnard, J. Phys. C **6**, 1709 (1973).
[29]I. Levin, V. Krayzman, J. C. Woicik, A. Tkach, and P. M. Vilarinho, Appl. Phys. Lett. **96**, 052904 (2010).